INVESTIGATION OF THERMAL LOADS ON HYPERSONIC VEHICLES WITH EMPHASIS ON SURFACE RADIATION EFFECTS

R.K. Höld and L. Fornasier

Deutsche Aerospace AG, Military Aircraft Division
D-81663 Munich, Federal Republic of Germany

Abstract

The prediction of accurate thermal loads is a major task during the development phase of hypersonic vehicles. Besides thermochemical effects, which are more significant for reentry conditions, the radiation of heat flux from hot surfaces can and does play an important role in the prediction of surface temperature distribution for cruising vehicles at hypersonic flight conditions. The radiation of energie from hot surfaces to infinity acts as a 'cooling system' and is a well known boundary condition in CFD. On the other hand, the phenomena of direct radiation which is neglected in classical approaches leads to increasing wall temperatures. This direct radiation as an interference phenomena between parts of a configuration which lie in the region of sight is subject matter of this paper. The basic principles of direct radiation are shortly reviewed and numerical methods predicting the influence on thermal loads are described. Different levels of radiation modelling accuracy are presented and discussed. Navier-Stokes calculations for a generic double fin test case at hypersonic flight conditions predict surface local temperature increase up to about $\Delta T = 300K$ caused by direct radiation effects.

Introduction

In the development of hypersonic vehicles, either reentry or cruising configurations, it is necessary to determine the thermal loads in addition to the classical aerodynamic loads. Numerical methods can and do play an important role in this task, since it is not possible to simulate in experimental ground facilities all the design relevant hypersonic flow phenomena and especially to cover the wide range of flight parameters (Ma, Re, Kn...) which have a major impact on them.

Accurate prediction of thermal loads at hypersonic flight conditions requires not only accurate modelling of thermochemical effects, which are more relevant to reentry bodies, but also accurate modelling of radiation effects as demonstrated in this paper. Due to the radiation of energy from the vehicle surface which is usually very hot in hypersonic flight, compared to the surrounding, the heat loads are decreased considerable. For the convex parts of the configuration it can be assumed that the radiation of energy is emitted through the transparent gas to infinity. For concave surfaces (junction at wings, intakes, fins), however, the balance of the heat loads is influenced considerably by direct radiation (radiation interference with other parts of the configuration which lie in the region of sight, see fig. 1). Of course, this only holds for high surface temperatures, because the effects are diminishing rapidly for decreasing temperatures.

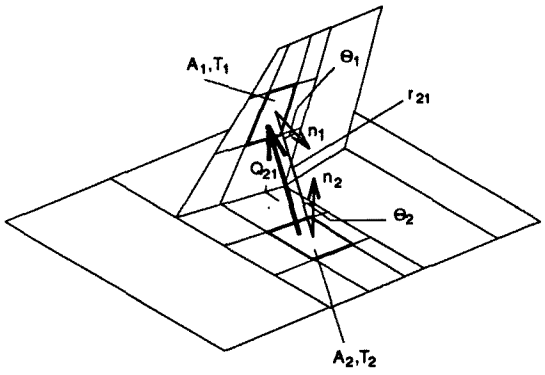

Fig. 1: Direct radiation phenomena

The emphasis of this study is on the determination of more accurate heat loads using direct radiation modelling. For this purpose the basic principles of direct radiation are reviewed and a model describing its influence on surface temperature distribution is presented. To describe direct radiation effects a fictitious emissivity coefficient, related to the well known emissivity coefficient, is defined. Different levels of radiation modelling accuracy can be considered. In the simplest option radiation models are not coupled to the flow field solution. This gives trends on the influence of direct radiation. This simple model is easily and very efficiently combined with Euler/boundary-layer or approximate solvers. The most complex model discussed is coupled directly with the Navier-Stokes solver NSFLEX [1, 2, 3].

Direct radiation modelling

Basic principles of direct radiation

Direct radiation is the energy transport of heat flux between parts of configurations which lie in the region of sight as demonstrated in fig. 1 (see [4] et al). Every surface element of the configuration radiates a heat flux depending of its surface temperature and the emissivity coefficient as described below. This heat flux can interact with other radiating surface elements. In fig. 1 the energy transport Q_{21} of a radiating surface element A_2 to the surface element A_1 is shown. Vice-versa the surface element A_1 radiates the rate of energy Q_{12} to the panel A_2. The behaviour of the air between the surface panels can be modelled by transparent gas assumption up to flight velocities of about $10km/s$, related to relevant hypersonic flow field conditions (see [5]). The assumption of a transparent gas means that there is no radiation and no absorption of energy in air particles itself, and the coupling of the direct radiated energy with the flow field is given by the temperature profile of the boundary layer only. The influence of a absorbing and radiating gas should be discussed for the thermal design of aeroassisted orbital transfer vehicles for example, but this is not subject of this paper. In the following the transparent gas assumption is used.

The solid surface elements A_1 and A_2 are characterized by the temperatures T_1 and T_2 and the normal vectors $\underline{n}_1$ and $\underline{n}_2$. Assuming total visibility of the surface elements A_1 and A_2, the distance r_{21} of the elements and the angles Θ_1 und Θ_2 define the rate of energy Q_{21} radiated from A_2 and acting on A_1:

$$Q_{21} = \frac{\epsilon\,\sigma}{\pi} \iint \frac{{T_2}^4 \cos\Theta_1 \cos\Theta_2}{{r_{21}}^2}\, dA_1 dA_2. \qquad (1)$$

The inverse energy transport Q_{12} from element A_1 to element A_2 is given by exchanging the indices of the variables in eq. 1. The emissivity coefficient ϵ describes the radiation characteristics of the solid surface element A_2 representing a nonblack body. The assumption of nonblack body behaviour is valid in this context and is based on a uniform emission and reflexion of rays with respect to angle of radiation and wavelenght. In the following, the emission coefficient is handled as a material constant valid for all solid surface elements A_i. This assumption holds for most of the investigated configurations. The algorithm, however, can handle local varying emissivity coefficients as well as global coefficients. σ is the Stefan–Boltzmann constant $(5.67 \cdot 10^{-8}\, W/(m^2 K^4))$. Integrating the energy transport (eq. 1) of a element A_2 to the surrounding, which is represented by a hemisphere, yields the well known Stefan–Boltzmann law

$$Q_{2\infty} = \sigma\,\epsilon\,{T_2}^4 A_2.$$

The heat flux q_{12} impinging the surface element A_1 is given by

$$q_{21} = Q_{21}/A_1 \qquad (2)$$

which represents the rate of energy transport related to a reference area. In the following, the reference area is the area of the solid surface element the heat flux is impinging on.

To find the thermal load at a solid surface element we have to look for the absorbed heat flux at this element. As stated by the radiation law of Kirchhoff we assume the absorption coefficient α to be equal to the emission coefficient ϵ. This is usually valid for nonblack bodies with a uniform emission and reflection of rays as discussed above. The absorbed heat flux at surface element A_1 caused by the energy rate Q_{21} is consequently given by

$$q_{1,ab} = -\,\epsilon\, q_{21}. \qquad (3)$$

Beside this absorption of energy the solid surface element A_1 emits the heat flux

$$q_{1,em} = \epsilon\,\sigma\,{T_1}^4$$

which depends on the temperature of the surface element. The sum of absorbed and emitted heat flux is the thermal load coming along with radiation effects:

$$\Delta q_1 = q_{1,ab} + q_{1,em} = \epsilon\,(\sigma\,{T_1}^4 - q_{21}). \qquad (4)$$

Diffuse Reflexion

The heat flux between nonblack bodies is influenced by another phenomena, the diffuse reflexion which causes additional heat loads. The diffuse reflexion phenomena and the related heat fluxes are sketched in fig. 2.

The figure depicts the successive reflexion of an emitted ray between the finite surface elements dA_1 and dA_2 with the related temperatures T_1 and T_2. Using the definition of a view factor

$$F := \frac{1}{\pi} \iint \frac{\cos\Theta_1\, \cos\Theta_2}{{r_{21}}^2} dA_1 dA_2 \qquad (5)$$

which describes the geometrical aspects of the radiation phenomena, the rate of energy dQ_{12} from eq. 1 is given by

$$dQ_{12} = \epsilon\,\sigma\,{T_1}^4 F = q_1\, F. \qquad (6)$$

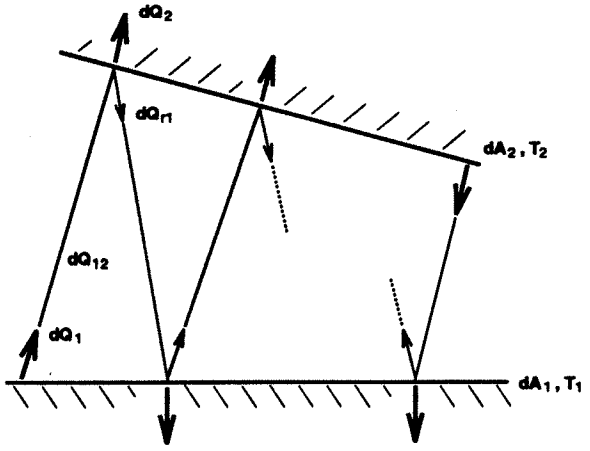

Fig. 2: Radiation phenomena between nonblack surfaces

dQ_1 is the rate of energy that is emitted from the surface element dA_1 to the surrounding, the related heat flux is given by

$$q_1 = \epsilon\,\sigma\,{T_1}^4.$$

dQ_{12} is the component of dQ_1 which impinges element dA_2. From eq. 6 we can see that dQ_{12} is the product of the view factor F and the emitted rate of energy dQ_1.

Fig. 2 shows emitted, reflected and absorbed rates of energy for both surface elements. First we will follow the ray starting from face dA_1. The emitted rate of energy is

$$dQ_1 = \epsilon\,\sigma\,{T_1}^4\,dA_1 = q_1\,dA_1.$$

dQ_{12}, as the rate of energy impinging dA_2, is split at dA_2 into a reflected part and an absorbed part. The absorbed rate of energy is given by

$$dQ_2 = -\epsilon\,q_1\,F = -\,\epsilon^2\,\sigma\,{T_1}^4\,F,$$

and the reflected component is

$$dQ_{r1} = (1-\epsilon)\,q_1\,F = (1-\epsilon)\,\epsilon\,\sigma\,{T_1}^4\,F.$$

The reflected ray again impinges face A_1 and starts another splitting procedure. Each splitting reduces the reflected rate of energy by $F\cdot(1-\epsilon)$. Although there is a infinite number of reflexions the component of heat load caused by reflected rays decreases rapidly for small values of $F\cdot(1-\epsilon)$.

Another reflexion process is started from the heat flux $q_2 = \epsilon\sigma{T_2}^4$, emitted from face dA_2 as shown in fig. 2 on the right. The overall heat load at face dA_1 is the sum of all the emitted and absorbed heat fluxes at face dA_1. Reflected components of rays do not have any influence on this heat flux integral. This yields the heat flux integral, caused by reflexion effects, as

$$dq_{(dA1)} = dQ_{(dA1)}/dA_1 =$$

$$= q_1\left[1-\epsilon\sum_{i=1}^{\infty}(1-\epsilon)^{2i-1}\left(\frac{F^2}{dA_1dA_2}\right)^i\right] - \quad (7)$$

$$-q_2\,\frac{\epsilon F}{dA_1}\left[1+\sum_{i=1}^{\infty}(1-\epsilon)^{2i}\left(\frac{F^2}{dA_1dA_2}\right)^i\right]$$

with $q_1 = \epsilon\sigma{T_1}^4$ and $q_2 = \epsilon\sigma{T_2}^4$. From eq. 7 we see that direct radiation is a function of the emissivity coefficient ϵ, the wall temperature distribution T_{wall}, the geometry of the configuration, and the visibility conditions of surface elements, i.e.:

$$dq_{(dA1)} = \mathcal{F}(\epsilon, T_{wall}, geometry, visibility).$$

Writing eq. 7 in orders of magnitude with respect to $(1-\epsilon)$ and F we find

$$dq_{(dA1)} = q_1 - q_2\,\frac{\epsilon F}{dA_1} - q_1\,\epsilon\,(1-\epsilon)\,\frac{F^2}{dA_1dA_2} + \\ + O\left(\left((1-\epsilon)\frac{F^2}{dA_1dA_2}\right)^2\right). \quad (8)$$

The first term q_1 on the right hand side of eq. 8 represents the emitted heat flux of face A_1, the second term is the absorbed part of the ray emitted from A_2, and the third term is related to the first reflexion of the ray starting at face A_1. This three terms are calculated by the described code. The calculation of additional terms would require tremendous computational effort compared to the first three terms. Only a vanishing influence of the third and the following terms on the results obtained was detected up to now. This comes along with relevant emissivity coefficients in the order of $\epsilon = 0.8$ and typically small view factors F. The results presented in this paper are calculated using the first two term of eq. 8. A difference to results retaining the third term is not visible. The third term, as a heat flux caused by reflected rays, can become of interest especially in combination with highly reflecting materials (i.e. small ϵ) and/or configurations with great view factors (e.g. internal flow field calculations).

Fictitious emissivity coefficient

Classical CFD methods usually make different options for boundary conditions with respect to the wall heat flux or to the wall temperature available. One of this options, the radiation–adiabatic surface, is often used in combination with hypersonic flow field calculations to have a more realistic prediction of heat loads compared to defined wall temperature or adiabatic wall

assumptions (see [6]). An radiation–adiabatic surface is defined by the equilibrium of the emitted heat flux of the surface and the wall heat flux coming from the temperature gradient in the boundary layer:

$$\epsilon \sigma T_1^4 = -k \left(\frac{\partial T}{\partial n}\right)_w. \qquad (9)$$

The radiated heat flux depends on the emissivity coefficient ϵ which is a material constant in the classical approach. The values of ϵ can range from $\epsilon = 0$ for totally reflecting surfaces to $\epsilon = 1$ for black bodies. Setting $\epsilon = 0$ in eq. 9 is equivalent to the adiabatic wall condition and leads to an overprediction of surface temperatures compared to realistic flight data. High values of ϵ can reduce wall temperatures for some hundreds of K at hypersonic flight conditions. Typical emissivity coefficients are $\epsilon \approx 0.8$.

In the following a new definition of a emissivity coefficient is presented which makes use of the widespread radiation–adiabatic surface option of CFD methods. With this definition the extension of many CFD codes for taking direct radiation into account is an easy job to do. The material constant ϵ in eq. 9 is replaced by a local value ϵ_f, named the 'fictitious emissivity coefficient'. There is no change in boundary condition handling, compared to the radiation–adiabatic surface condition. The fictitious emissivity coefficient ϵ_f includes the direct radiation effects as well as the radiation of heat flux from the surface to infinity defined by the material constant ϵ. The difference of ϵ_f and ϵ indicates the influence of direct radiation effects.

Analogous to the Stefan–Boltzmann law the fictitious emissivity coefficient is introduced as

$$\epsilon_f := \frac{\Delta q_1}{\sigma T_1^4} \qquad (10)$$

with the heat flux Δq_1 as the numerical result of eq. 7 for the surface element ΔA_1, with regard on all elements ΔA_2 which are visible to ΔA_1. Using this definition the following statements characterize the present approach:

- easy to implement modelling of direct radiation effects for all CFD methods already using radiation–adiabatic boundary conditions:

  the material constant ϵ is replaced by the local fictitious emissivity ϵ_f,

- easy to interpret local influence of direct radiation:

$\epsilon_f \approx \epsilon$	$\Longrightarrow$	direct radiation can be neglected,
$\epsilon_f = 0$	$\Longrightarrow$	adiabatic boundary condition,
$\epsilon_f < 0$	$\Longrightarrow$	$q_{1,absorbed} > q_{1,emitted}$.

The interpretation of the fictitious emissivity coefficients directly shows the influence of direct radiation on the wall heat flux as sketched in the table. If $\epsilon_f \approx \epsilon$ direct radiation can be neglected, $\epsilon_f = 0$ is encountered if the absorbed heat flux equals the emitted heat flux, and negative values of ϵ_f occur if the absorbed heat flux exceeds the emitted heat flux. The heat loads and the related wall temperature distribution depend on the fictitious emissivity coefficients as follows: with decreasing ϵ_f the heat loads and wall temperatures increase and vice-versa.

There is no explicit limits for ϵ_f but for the maximum of ϵ_f. Surface elements that are not impinged by rays are characterized by $\epsilon_f = \epsilon$, the overall maximum for ϵ_f. The minimum of ϵ_f depends on the geometry of the configuration and the flow field solution. Energy balance considerations and the physical behaviour of radiation shows that the maximum wall temperature level remains limited.

Numerical method

Navier–Stokes method

The Navier-Stokes method used to investigate the direct radiation effects is the finite-volume solver NSFLEX developed at Dasa. It solves both the full and the thin-layer Navier–Stokes equations as well as the Euler equations [1, 2, 3].

The governing equations are the time dependent Reynolds-averaged compressible Navier–Stokes equations in conservative form. To reach the steady state solution the equations are solved in time-dependent form. For the time integration an implicit relaxation procedure for the unfactored equations is employed which allows large time steps [7]. A Newton method is used, constructed by linearizing the fluxes about the known time level. The system of equations resulting from the discretization is solved approximately at every time step with a Jacobi or Gauss-Seidel relaxation. The time step is calculated with the maximum of the eigenvalues of the inviscid Jacobians. As an example, the CFL number used for the calculation presented here is 1000. Three Jacobi steps are performed at every time step.

To evaluate the inviscid fluxes a linear locally one-

dimensional Riemann problem is solved at each volume face, whereby spatial discretization up to third-order accurate is used. An hybrid local characteristic and Steger–Warming type scheme is employed, which allows the code to work for a wide range of Mach numbers [8]. Van Albada type sensors are used to detect discontinuities in the solution. To calculate the local characteristic fluxes, the conservative variables on both sides of each volume face are extrapolated up to third order in space (MUSCL type extrapolation). This scheme guarantees the homogeneous property of the Euler fluxes, hence simplifying the evaluation of the true Jacobians of the fluxes for use on the left-hand side [1].

Because this local characteristic flux is not diffusive enough to guarantee stability for hypersonic flow cases, especially in the transient phase where shocks are moving, an hyper-diffusive flux formulation is used locally in regions with high gradients. This is a modified Steger-Warming type (flux vector splitting) flux which gives good conservation of the total enthalpy. Diffusive fluxes at the cell faces are calculated with central differences [7].

A simple approach to account for equilibrium real gas effects is incorporated which allows the Riemann solver and the left–hand side of the flow solver to remain unchanged. The test case calculations are done for perfect gas assumption. For more information about the equilibrium real gas modelling see [2, 3, 8, 9, 10].

At the farfield boundaries non-reflecting boundary conditions are inherent in the code since the code extracts only such information from the boundary which is allowed by the characteristic theory. At outflow boundaries, as long as the flow is supersonic, the code does not need information from downstream. In the part of the viscous regime where the flow is subsonic the solution vector is extrapolated constantly. No upstream effect of this extrapolation could be observed up to now.

At solid bodies the no-slip condition holds. Several temperature and heat flux boundary conditions are incorporated: adiabatic wall, given wall heat flux, fixed wall temperature and different levels of radiation modelling at solid surfaces. The different radiation modelling levels are based on the outlined theory and discussed in the following.

Direct radiation modelling

The implementation to calculate the direct radiation effects is done in a two step modular way. The first module, named 'VISIC', is a method searching and defining all the visibility connections for all of the surface elements of the configuration. This module detects geometrical dependencies and is called in a preprocessing loop. No flow field data or free stream conditions are handled in VISIC and the module is called once for each configuration of interest. The number of operations necessary in VISIC to find the visibility information is a square function of the number of surface elements. Compared to the processing time for the Navier-Stokes solution the processing time in the module VISIC remains small. Applying direct radiation modelling to approximate methods, should increase processing time moderatly, due to the usually coarse grids used with approximate solvers compared to Navier-Stokes calculations. The visibility information for the presented double fin test case with about 4000 surface elements was calculated on an IBM-Risc 6000 workstation.

The second module, named 'DIRAD' makes the fictitious emissivity coefficients ϵ_f available. The module DIRAD is called by the Navier-Stokes solver depending on the level of direct radiation modelling accuracy. Three levels of direct radiation modelling accuracy are investigated

1. $\epsilon_f = \mathcal{F}(geometry)$,
2. $\epsilon_f = \mathcal{F}(geometry, T(\epsilon))$ and
3. $\epsilon_f = \mathcal{F}(geometry, T)$.

In the simplest option 1 the wall temperature of the surface elements in module DIRAD is assumed to be constant. The calculation of ϵ_f by DIRAD becomes independent of the flow field solution, no iteration procedure for DIRAD is necessary. The values of ϵ_f represent view factors in this case. This level of radiation modelling accuracy do not need any flow field solutions and can give trends on the influence of direct radiation as shown by the test case calculations.

The medium level option 2 uses an assumed wall temperature distribution in module DIRAD. The assumed wall temperature distribution in DIRAD decouples the direct radiation modelling from the flow field solver. The computional effort is nearly the same for option 1 and 2, but option 2 can handle a more realistic wall temperature distribution compared to option 1. The fictitious emissivity coefficients of op-

tion 2 combine view factors with the influence of an assumed wall temperature distribution.

The highest level of radiation modelling accuracy (option 3) calculates ϵ_f as a function of not only the geometrical data, but also as a function of the actual wall temperature within an iterative procedure of the flow field solver. This approach is the most expensive but also the most realistic one. The results presented demonstrate the need to use this highest level of radiation modelling for accurate solutions with respect to the prediction of wall temperature distributions.

The physical behaviour of the direct radiation problem is of elliptic type in space. This comes from the coupling of surface elements by direct radiation. To use the highest level option 3 in combination with approximate solvers which usually can not handle the elliptic coupling in space, means to run some complete solutions with an iterative update of the wall temperature data in DIRAD. Within Navier-Stokes solutions, however, the actual wall temperature is available at every iteration level and the extra processing time for an update of ϵ_f remains moderate. In this context the Navier-Stokes test case calculations indicated that an update of ϵ_f is not necessary at every iteration level reducing the extra processing time significantly.

During development of the direct radiation modelling the modules DIRAD and VISIC were investigated for a number of generic test cases. These generic test cases demonstrate that accurate solutions for the direct radiation problem needs fine paneling especially in corner regions of a configuration. The module DIRAD uses automatic mesh refinement, which can be controlled by input parameters, to raise the accuracy of the solution in corner regions.

Results

For the investigation of direct radiation effects, typical for hypersonic cruising vehicles, a generic double fin test case was defined. The surface grid consisting of about 4000 panels is plotted in fig. 3. The space grid is being built by 7 blocks with an overall number of 75 000 finite volumes. Free stream conditions were defined, representing relevant hypersonic flow field conditions: $Mach = 7$, $\alpha = -5°$, $altitude = 27km$, $reference\ length = 7m$, $Re = 4.3 \cdot 10^7$. Laminar flow is investigated. The full Navier–Stokes equations for perfect gas are solved. The angle of attack of $\alpha = -5°$ generates a shock lying outside of the fins.

Fig. 4 shows the fin region of the configuration with

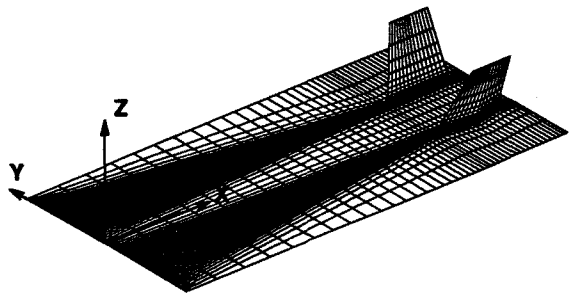

Fig. 3: Surface grid of the double fin test case

x=const. and y=const. cuts. Along these cuts temperature data is plotted for different levels of radiation modelling accuracy. All geometric data is given in dimensionless coordinates with a reference length of the overall body length. The temperature data at x=const. is presented in different graphs for the inner region and the outer region of the double fin test case as shown in fig. 5.

As reference solutions two calculations neglecting direct radiation are presented. These two solutions assume constant radiation with

$$\epsilon = 0.85 \text{ and } \epsilon = 0.40$$

at the surface. To demonstrate the influence of direct radiation modelling the three different levels, as outlined in the previous section, are investigated:

$$\begin{aligned} \epsilon_f &= \mathcal{F}(geometry), \\ \epsilon_f &= \mathcal{F}(geometry, T(\epsilon = .85)) \text{ and} \\ \epsilon_f &= \mathcal{F}(geometry, T). \end{aligned}$$

All of these three calculations assume an emissivity coefficient of $\epsilon = 0.85$. The medium level calculation (option 2) with $\epsilon_f = \mathcal{F}(geometry, T(\epsilon = .85))$ is based on a temperature distribution for module DIRAD obtained from the reference solution with $\epsilon = 0.85$.

The figs. 6 to 9 compare the solutions for temperature distribution at y=const. The reference solutions ($\epsilon = 0.85$ and $\epsilon = 0.40$) differ in a nearly constant offset of about $T = 150K$. The maximum outside of the fins is produced by the shock which is generated at the leading edge of the fin. The higher temperature level of the $\epsilon = 0.40$ calculation comes along with the reduced emission of heat flux compared to the $\epsilon = 0.85$ solution. The temperature difference between the highest level of radiation modelling $\epsilon = \mathcal{F}(geometry, T)$ and the reference solution $\epsilon = 0.85$ in figs. 6 and 7 is caused by direct radiation. Up to $x \approx 0.6$ the influence of direct radiation is vanishing, in the fin region, however, direct radiation effects increase the temperature up to

$\Delta T \approx 200K$. Although the calculation $\epsilon = 0.40$ is a kind of worst case for this test case, there is a great difference to the $\epsilon = \mathcal{F}(geometry, T)$ - solution. The three direct radiation models in figs. 8 and 9 show for the temperature an underprediction of the lowest level modelling $\epsilon = \mathcal{F}(geometry)$ and a very large overprediction of the medium level modelling $\epsilon = \mathcal{F}(geometry, T(\epsilon = 85))$ compared to the highest level modelling $\epsilon = \mathcal{F}(geometry, T)$. The low level modelling shows the influence of geometrical aspects and gives trends for the influence of direct radiation. The medium and high level models manifest the significant dependency of the direct radiation heat loads from the wall temperature distribution. The strong coupling of wall temperature distribution and direct radiation heat fluxes in the high level modelling reduces surface temperatures compared to the medium level solution. This comes along with the 'heating of cold surface elements by hot elements and the cooling of hot elements by cold elements'.

Temperature profiles at x=const. are plotted in figs. 10 to 17. The differences for the three levels of direct radiation modelling are small at the fin faces compared to the fuselage. This is caused by the low heat flux emitted from the relative cool fuselage panels compared to the fin panel radiation ($q \sim T^4$). Fig. 17 is an example showing a tremendous overprediction of temperature by the medium level radiation model in regions of high temperature gradients.

Isoline presentations of the temperature distribution for the reference solution $\epsilon = 0.85$ and the highest level of radiation modelling are shown in figs. 18 and 19. As inferred from the previous figures, direct radiation increases the wall temperature in wide regions of the fuselage. There is a great difference of both solutions for the wall temperature at the outside faces of the fins, especially in corner regions. Compared to this, the influence of direct radiation on the wall temperature at the inner faces of the fins is weak.

The fictitious emissivity coefficients ϵ_f calculated for the three levels of radiation modelling accuracy are presented in figs. 20 to 22. The smooth distribution of ϵ_f for the low level model (fig. 20) compared to the medium level (fig. 21) and high level modelling (fig. 22) again demonstrates the strong coupling of direct radiation with the wall temperature. The medium level calculation produces negative values of the fictitious emissivity coefficient ϵ_f which leads to the stated overprediction in temperature distribution. The solution with the highest level of radiation modelling accuracy predicts values for the fictitious emissivity coefficient in the range of about $0.2 < \epsilon_f < 0.85$.

Conclusions

The basic principles of direct radiation were presented and the general radiation problem was formulated. The definition of a fictitious emissivity coefficient leads to an easy to implement procedure to handle direct radiation effects in numerical methods. The coupling of the different radiation models to the Navier–Stokes solver NSFLEX showed no negative influence on the overall numerical scheme.

Presented results and other results from the work done in the frame of the German Hypersonic Technology Program show that there is the need to use direct radiation modelling for accurate solutions and the prediction of wall temperature distribution in hypersonic flight regimes. This comes along with the strong coupling of wall heat flux caused by radiation effects with the temperature profile of the boundary layer flow. All the models used for calculation of direct radiation predict an increase of surface temperature up to about $300K$ in the fin region.

Three different levels of direct radiation modelling accuracy were investigated. Only the most complex level of direct radiation modelling seems to result in an accurate solution. The lowest level of radiation modelling typically underpredicts the wall temperature, whereas the medium level of radiation modelling leads to an overprediction of the wall temperature as demonstrated for the double fin test case.

Because of lack of comparison with other source data obtained results cannot be regarded as quantitatively validated, but the qualitative behaviour of results appear to be in line within underlying physics.

References

[1] Schmatz, M. A. : NSFLEX – an implicit relaxation method for the Navier–Stokes equations for a wide range of mach numbers. In Wesseling, P., editor, *Numerical Treatment of the Navier–Stokes Equations*, pp. 109–123, Kiel, 1989. Vieweg. Proc. of the 5^{th} GAMM–Seminar, NNFM Vol. 30.

[2] Schmatz, M. A. : Hypersonic three–dimensional Navier–Stokes calculations for equilibrium air. *AIAA–paper 89–2183*, 1989.

[3] Schmatz, M. A.; Hölđ, R. K.; Monnoyer, F.; Mundt, Ch. and Wanie, K. M. : Numerical methods for aerodynamic design II. *Space Course Aachen, paper no. 62*, 1991. Also MBB–FE211–S–PUB–442.

[4] Bird, R. B.; Stewart, W. E. and Lightfoot, E. N. :

Transport Phenomena. John Wiley & Sons, New York, 1960.

[5] Höld, R. K. : *Die Berechnung dreidimensionaler Hyperschallströmungen mit Hilfe der Viscous-Shock-Layer-Gleichungen.* Fortschritt-Berichte, Reihe 7, Nr. 171. VDI, Düsseldorf, 1990.

[6] Hirschel, E.H.; Koç, A. and Riedelbauch, S. : Hypersonic flow past radiation-cooled surfaces. *AIAA paper 91-5031*, 1991. Also MBB-FE202-S-PUB-468.

[7] Schmatz, M. A. : Three-dimensional viscous flow simulations using an implicit relaxation scheme. In Kordulla, W., editor, *Numerical simulation of compressible viscous-flow aerodynamics*, pp. 226-242. Vieweg, 1988. Notes on Numerical Fluid Mechanics, Vol. 22.

[8] Eberle, A. : Characteristic flux averaging approach to the solution of Euler's equations. In *VKI lecture series 1987-04*, 1987.

[9] Mundt, Ch.; Keraus, R. and Fischer, J. : New, accurate, vectorized approximations of state surfaces for the thermodynamic and transport properties of equilibrium air. *ZfW 15*, pp. 179-184, 1991.

[10] Mundt, Ch.; Monnoyer, F. and Höld, R. K. : Computational Simulation of the Aerothermodynamik Characteristics for the Reentry of HERMES. *AIAA-paper 93-5069*, 1993. Also DASA-LME211-S-PUB-528.

Figures

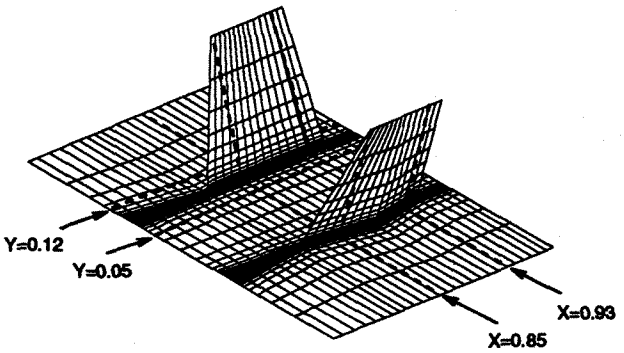

Fig. 4: Fin region of the investigated configuration

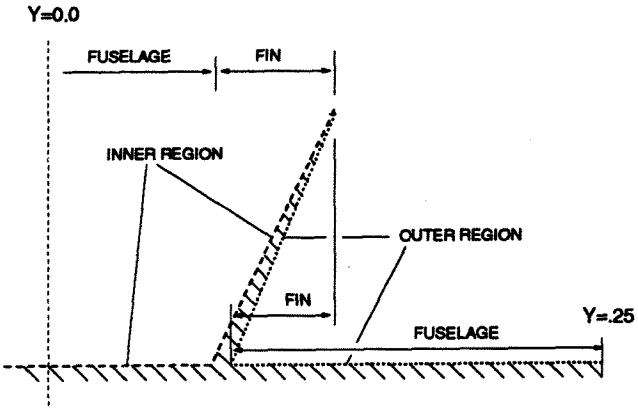

Fig. 5: x=const. cut in the fin region

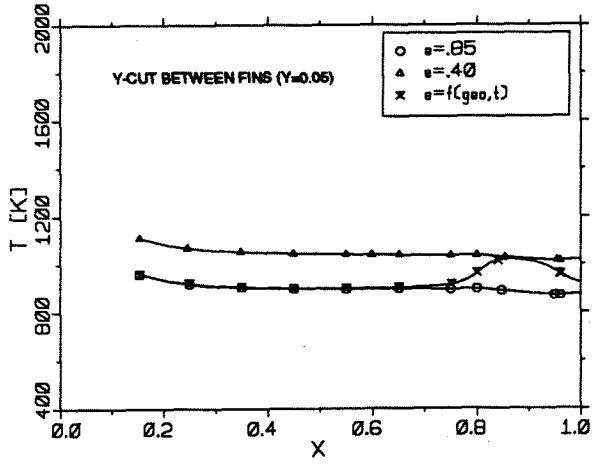

Fig. 6: Temperature distribution at y=0.05, reference solutions

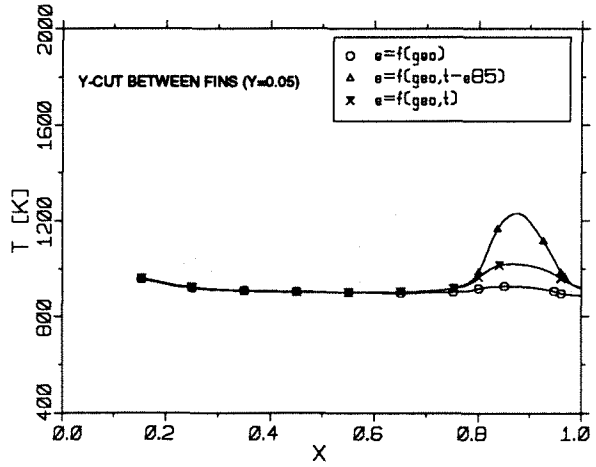

Fig. 7: Temperature distribution at y=0.05, direct radiation modelling

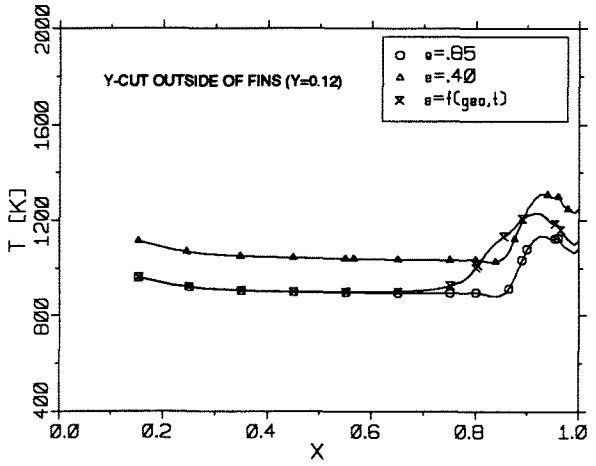

Fig. 8: Temperature distribution at y=0.12, reference solutions

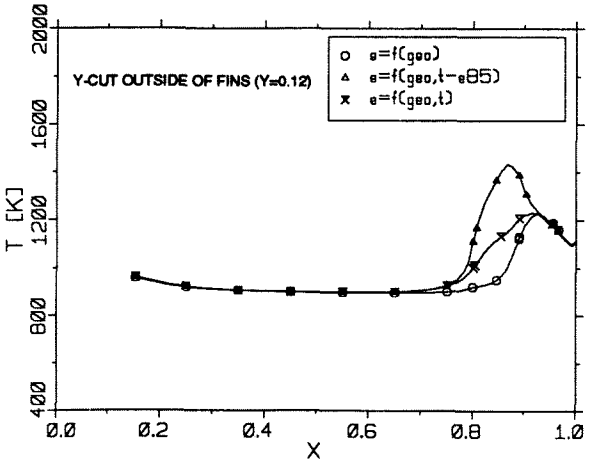

Fig. 9: Temperature distribution at y=0.12, direct radiation modelling

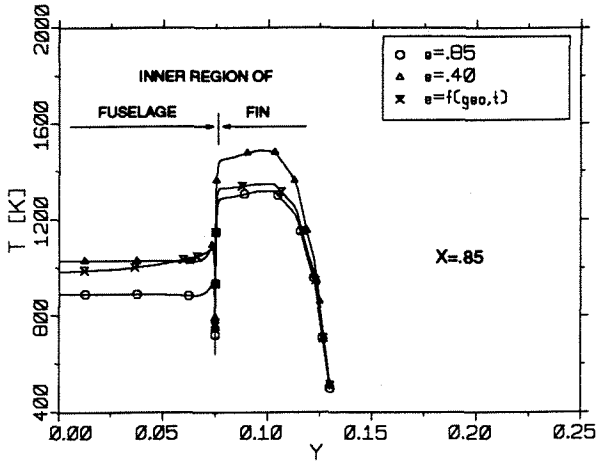

Fig. 10: Temperature distribution at x=0.85, inner fin region, reference solutions

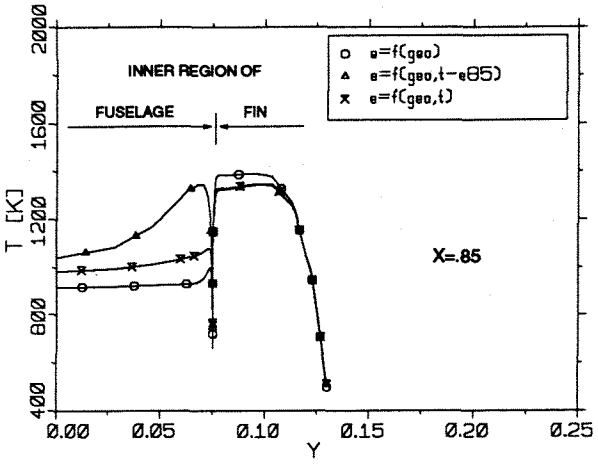

Fig. 11: Temperature distribution at x=0.85, inner fin region, direct radiation modelling

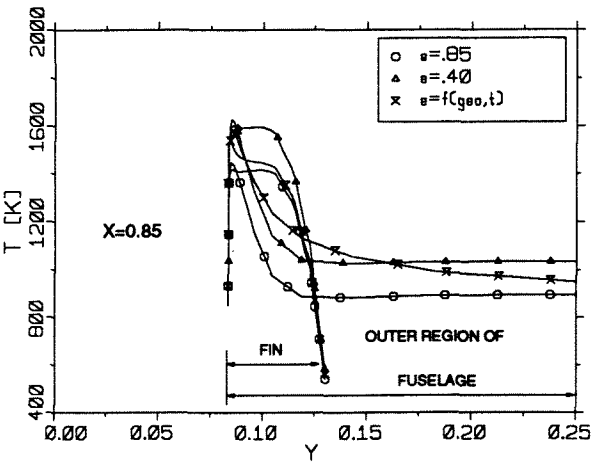

Fig. 12: Temperature distribution at x=0.85, outer fin region, reference solutions

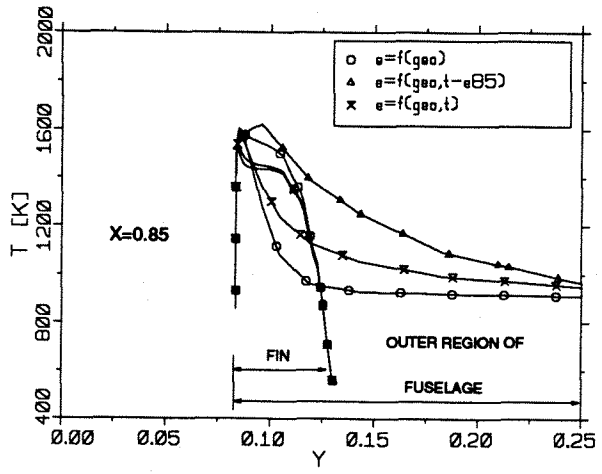

Fig. 13: Temperature distribution at x=0.85, outer fin region, direct radiation modelling

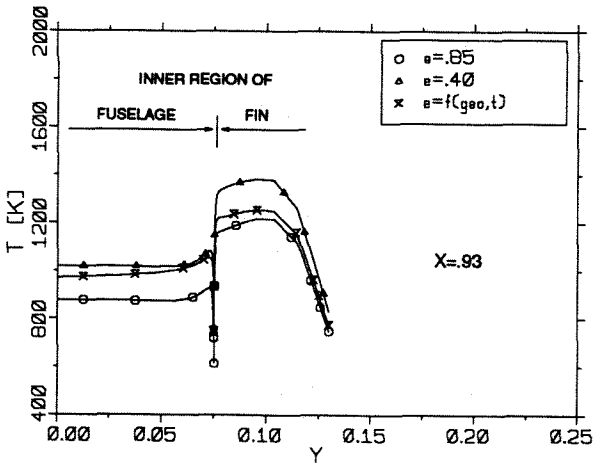

Fig. 14: Temperature distribution at x=0.93, inner fin region, reference solutions

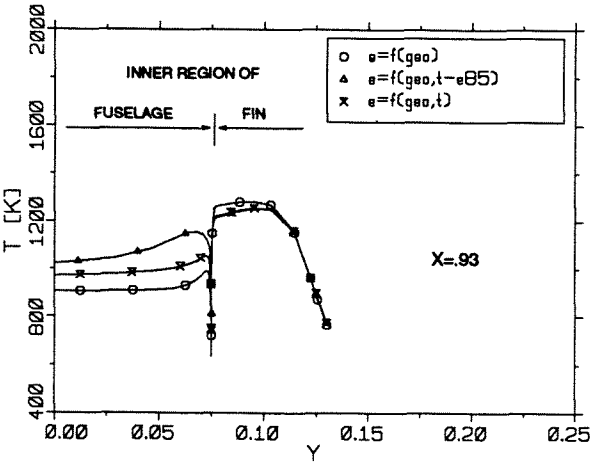

Fig. 15: Temperature distribution at x=0.93, inner fin region, direct radiation modelling

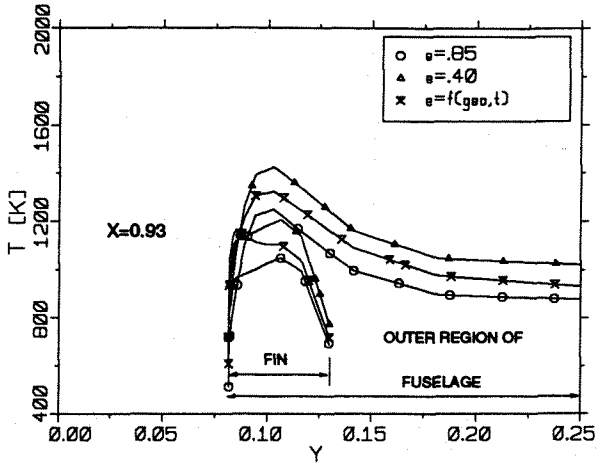

Fig. 16: Temperature distribution at x=0.93, outer fin region, reference solutions

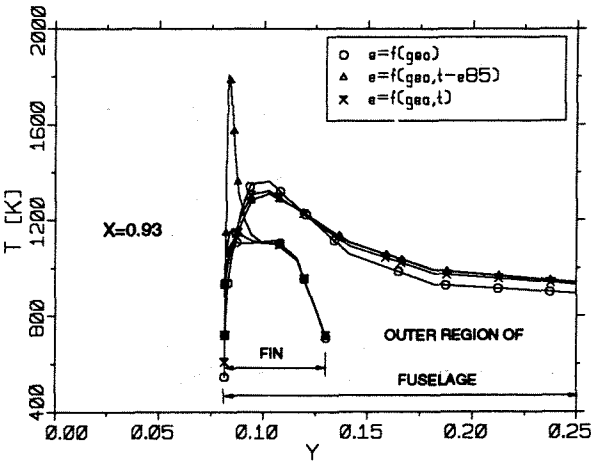

Fig. 17: Temperature distribution at x=0.93, outer fin region, direct radiation modelling

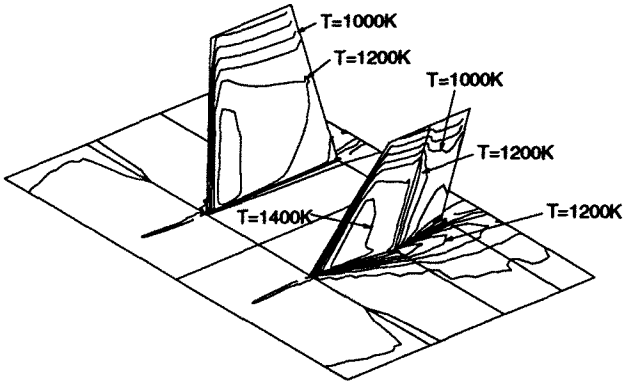

Fig. 18: Temperature distribution in the fin region, reference solution e=0.85

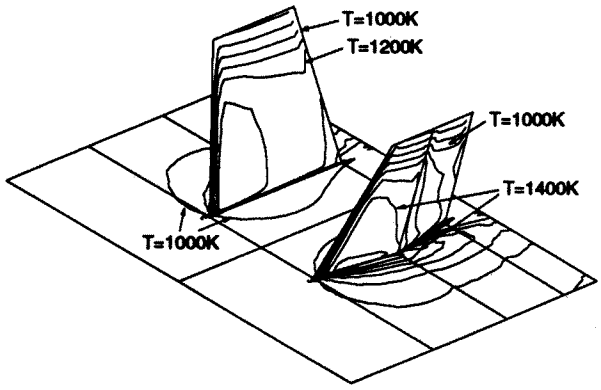

Fig. 19: Temperature distribution in the fin region, high level radiation modelling

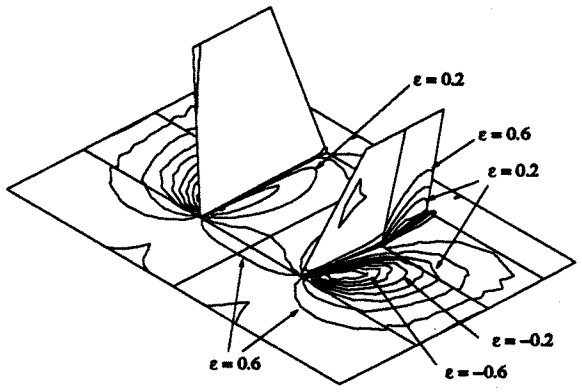

Fig. 21: Emissivity coefficient distribution in the fin region, medium level radiation modelling

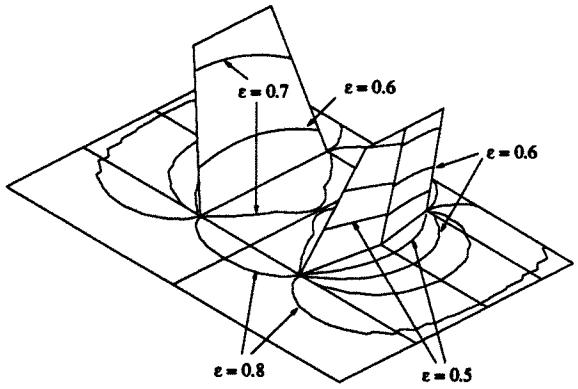

Fig. 20: Emissivity coefficient distribution in the fin region, low level radiation modelling

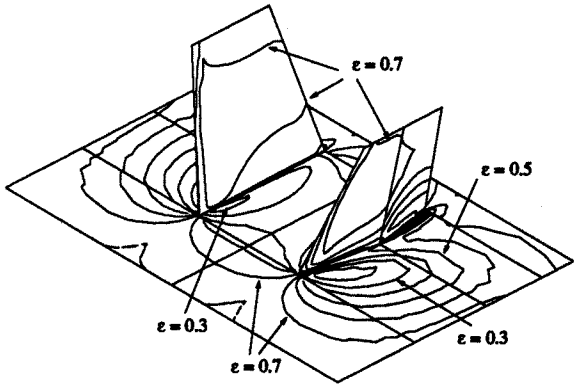

Fig. 22: Emissivity coefficient distribution in the fin region, high level radiation modelling